On the global relationship between polarimetric radio occultation differential phase shift and ice water content

Ramon Padullés[1,2], Estel Cardellach[1,2], and F. Joseph Turk[3]

[1]Institut de Ciències de l'Espai, Consejo Superior de Investigaciones Científicas (ICE-CSIC), Barcelona, Spain
[2]Institut d'Estudis Espacials de Catalunya (IEEC), Barcelona, Spain
[3]Jet Propulsion Laboratory, California Institute of Technology, Pasadena, CA, USA

Correspondence: Ramon Padullés (padulles@ice.csic.es)

Abstract. The Radio Occultations and Heavy Precipitation (ROHP) experiment aboard the Spanish PAZ satellite was deployed in 2018 with the objective of demonstrating the ability of Polarimetric Radio Occultation measurement (PRO) concept in detecting rain (liquid-phase precipitation). Analysis of these data has also demonstrated the ability of PRO to detect horizontally oriented frozen-phase precipitation. To verify these observations, a global climatological comparison is performed using the
5   Cloudsat (94-GHz) radar as a reference, for different heights and taking into account the radio occultation (limb-based) viewing geometry. A robust relationship (e.g. high correlation coefficient) is found between the polarimetric radio occultation observable differential phase shift ($\Delta\Phi$) and the integrated ice water content (IWC) along the rays, globally, and for heights above the freezing level. ~~The relationship is especially good over ocean, where~~ PAZ observations capture the major precipitation features and the signatures of the Inter-Tropical Convergence Zone ~~are well captured by the PAZ observations~~. The correlation
10   coefficients maximize for tropical-oceans, for a range of heights between 5 and 12 km. The ratios between $\Delta\Phi$ and along-ray integrated ~~ice water content are further evaluated~~ IWC mean climatologies are found to be within the range 0.03 - 0.09 mm kg^{-1} m^2, although uncertainty due to the IWC retrieval algorithm must be noted. Further evaluation of the ratios with single particle forward scattering simulations ~~, and the results~~ indicate that the scattering by frozen hydrometeors with a combination of effective densities, axis ratios and tilt angle distribution yield results that agree well with the observations. Overall,
15   the global climatological results obtained in this study show the presence of horizontally oriented particles across the whole globe, and for a wide range of height layers.

1 Introduction

The Radio Occultations and Heavy Precipitation (ROHP) experiment aboard the Spanish PAZ satellite (Cardellach et al., 2014) has demonstrated the ability of the polarimetric Radio Occultation (PRO) technique to complement well-established
20   RO processing techniques (e.g. Kursinski et al., 1997) with ~~a joint~~ the detection of heavy precipitation (Cardellach et al., 2019; Padullés et al., 2022). The detection is based on the total differential phase shift ($\Delta\Phi$) accumulated along the RO ray paths, traveling from the Global Positioning System (GPS) satellite emitter to the dual linearly polarized (H, V) receiver on the PAZ Low Earth Orbiter (LEO). Being a limb-sounding technique, the rays travel through deeper layers of the atmosphere as the occultation advances, penetrating into the layers where clouds and precipitation are expected. ~~The $\Delta\Phi$ is measured in~~

25 ~~mm and is obtained by comparing the electromagnetic phase at both antenna ports (e.g. $\Delta\Phi = \Phi_H - \Phi_V$), assuming that the phase measurements have been previously translated to optical length by the factor $\frac{\lambda}{2\pi}$.~~ This differential polarimetric phase measurement, in units of length, is set as the primary observable for PRO. It depends on the hydrometeors encountered along the rays as follows (Cardellach et al., 2014):

$$\Delta\Phi = \int_L K_{\mathrm{dp}}\mathrm{d}L \tag{1}$$

30 where K_{dp} is the differential phase shift ~~(mm/km)~~ and L is the traveled distance ~~(in km)~~. The K_{dp} is defined as:

$$K_{\mathrm{dp}} = \underline{10^3}\frac{\lambda^2}{2\pi}\int_D \Re\{S_{hh} - S_{vv}\}N(D)\mathrm{d}D \tag{2}$$

where λ is the wavelength (i.e. in the case of L-band GPS signals, $\lambda = 0.192$ m, corresponding to 1.575 GHz), $S_{hh,vv}$ are the co-polar components of the scattering amplitude matrix ~~(m)~~, and $N(D)$ is the particle size distribution ~~(m^{-4})~~ as a function of the equivalent particle diameter, D ~~(m)~~ i.e. the diameter of a sphere having the same mass.

35 K_{dp} contains the dependence of PRO observable on a series of microphysics parameters, such as the size, the shape and the amount of hydrometeors. The scattering amplitude matrix ($\mathbf{S}$, 2×2) provides information of the scattered field after propagating through an ensemble of hydrometeors. It depends on the shape and type of the hydrometeors (e.g. raindrops, pristine ice crystals, aggregate of ice particles, etc.). The dependence on the shape is often expressed in terms of the axis ratio, i.e. the ratio between the two main axis of the particle. For a perfectly spherical particle, $S_{hh} - S_{vv} = 0$. K_{dp} also depends on the size of

40 the hydrometeors ~~(generally directly linked to the shape and type)~~. This dependence on the size is proportional to its volume, and therefore it is affected by the third moment of the $N(D)$. The water content (WC) is also affected by the third moment of $N(D)$ as (e.g. Bringi and Chandrasekar, 2001):

$$\mathrm{WC} = \frac{\pi}{6}\rho_{\mathrm{w,i}}\int_D D^3 N(D)\mathrm{d}D \tag{3}$$

where $\rho_{w,i}$ is the density, typically of water or ice. Therefore, it is expected that there exists a relationship between K_{dp}

45 and WC. In fact, the use of K_{dp} to retrieve WC has been attempted before, for rain (e.g. Jameson, 1985) and for ice (e.g. Vivekanandan et al., 1994; Ryzhkov et al., 1998; Bukovčić et al., 2018; Nguyen et al., 2019) using radar at different frequencies ranging from S to K bands. However, in the case of ice and snow, there are additional factors that must be taken into account, namely, the percentage of horizontally oriented particles with respect to those that are randomly oriented, ~~and the associated~~ the effective density, and the shape and composition (i.e., dielectric constant of the ice/air media). In the case that all particles

50 were randomly oriented, the K_{dp} would cancel out regardless of the amount of WC.

Shape and orientation of ice particles have a direct relationship with the life-cycle of precipitation (e.g. Gong et al., 2020). Furthermore, ~~its knowledge~~ knowledge of shape and orientation is crucial for space-based retrievals of, for example, total ice

water paths (e.g. Kaur et al., 2022), and could help in the assimilation of passive microwave data in the all-sky assimilation schemes (e.g. Barlakas et al., 2021). In this regard, PRO observations have potential to help constraining the orientation of the

55 hydrometeors globally, with high vertical resolution. Other limb-sounding techniques, such as the Microwave Limb Sounder (MLS), have previously been used to sense ice particles (e.g. Wu et al., 2009) and constrain ~~its~~ their orientation (e.g. Davis et al., 2005), but ~~their~~ MLS vertical resolution is low.

In Padullés et al. (2022), the authors showed that the presence of horizontally oriented frozen particles is required in order to explain some of the PAZ PRO observations. In this new paper, we carry out an extensive analysis of the global relationships

60 between ~~water content~~ ice water content (IWC) and $\Delta\Phi$. To do so, a synthetic radio occultation mission is simulated based on ice water properties provided by the Cloudsat data products between 2006-2016. That is, a set of actual radio occultation rays are artificially placed overlaying the Cloudsat curtain-like observations, continuously thorough the whole period. In this way the Cloudsat observations, like radar reflectivity, and its retrievals, like ~~ice water content (IWC)~~IWC, can be analyzed as if they were observed in RO geometry. The statistics gathered from these observations would be equivalent to any other RO mission,

65 if this was able to measure such quantities.

This strategy arises from the fact that there are no coincident observations between the Cloudsat and PAZ, due to different orbit parameters. However, the artificially generated products enable us to compare, in a statistical or climatological way, the PAZ $\Delta\Phi$ observations with retrievals from Cloudsat, such as the IWC.

In this paper we focus on the spatial correlations between the IWC as would have been sensed by RO geometries in Cloudsat

70 measured backgrounds and the $\Delta\Phi$ from PAZ. If these two quantities are related, the spatial patterns should agree and the correlation should be high. This paper is therefore structured as follows: in Section 2 the artificial products based on Cloudsat retrievals and actual RO geometries are described. In Section 3 the correlations and relationship between the actual PAZ observations and the generated products are investigated. Finally, in Section 4, forward scattering simulations are used to validate and contextualize the relationships found in the previous section. The paper ends with a discussion on the findings.

75 ## 2 Cloudsat retrievals projected to RO geometries

The Cloudsat satellite was launched in April 28, 2006, and was regularly providing observations until August, 2020. It orbits at an approximate height of 715 km in a polar orbit (inclination of 98.2 deg) with an equatorial crossing time of about 1:30 PM. It carries a Cloud Profiling Radar (CPR) operating at 94 GHz (W-band) aimed at observing and characterizing clouds (Stephens et al., 2008). Its high frequency radar is particularly good at sensing the frozen part of clouds and precipitation, whereas it has

80 problems in penetrating to the lower altitudes in the deepest convective regions of precipitating systems (e.g. Battaglia et al., 2007). The parameters observed and retrieved from Cloudsat, of interest for this study, consist of the radar reflectivity (Z_e) in the 2B-GEOPROF product (Marchand et al., 2008), the IWC retrievals from the DARDAR product (Delanoë and Hogan, 2010) version 3 (Cazenave et al., 2019), and the IWC and particle size distribution parameters (N_t and σ) in the 2B-CWC-RO product (Austin et al., 2009). Auxiliary thermodynamic parameters such as temperature and humidity have been obtained from

85 the European Centre for Medium-range Weather Forecasts (ECMWF) model, provided along the IWC retrievals. All these
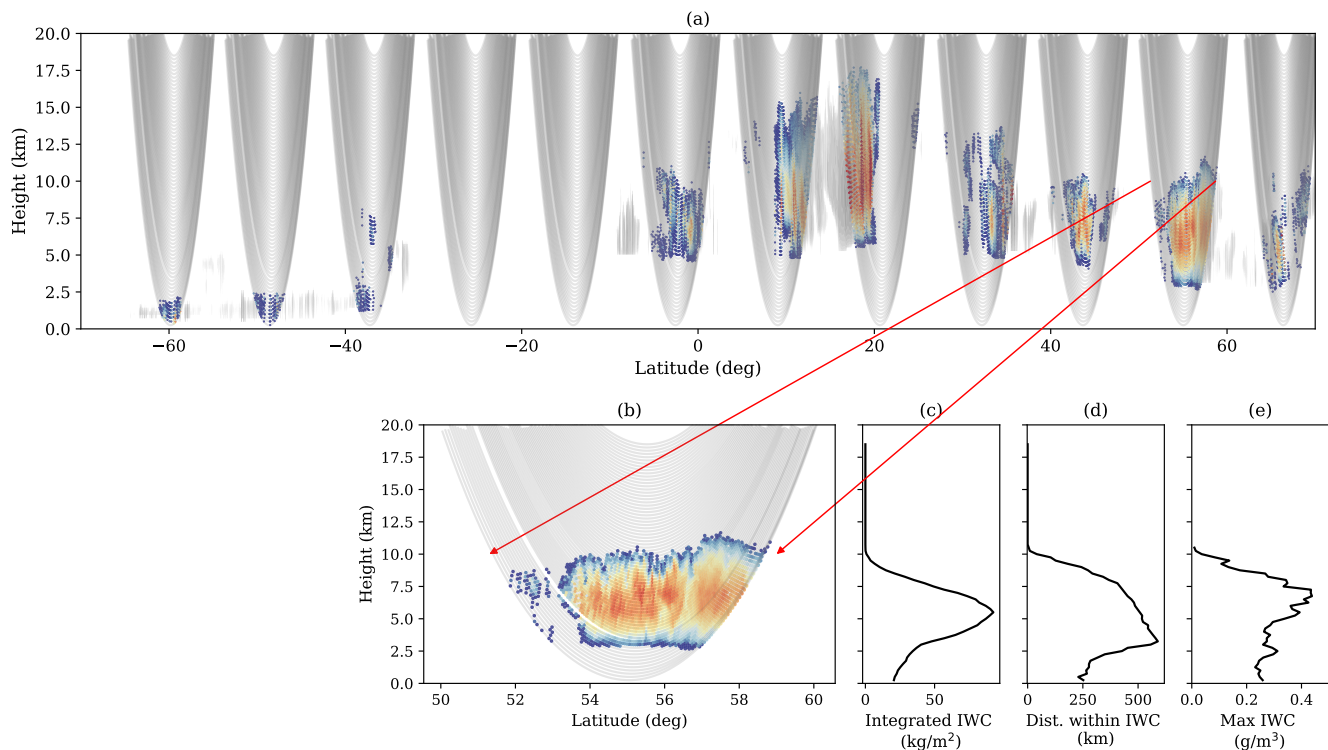
Figure 1. Example of half Cloudsat orbit observations (in this case, derived ice water content) with the RO rays overlapped. The Cloudsat orbit granule is 01075. In panel (a), only the Cloudsat ice water content being overlapped by RO rays are colored. IWC not being overlapped by RO rays are in gray-scale. Panel (b) shows a more detailed image of the Cloudsat derived ice water content interpolated into the RO rays, corresponding to one of the slices shown in panel (a) - indicated by the red arrows. In panels (c), (d), and (e) there is shown the corresponding integrated ice water content, distance traveled by the ray within the influence of IWC, and the maximum IWC encountered along the ray, respectively, as a function of each ray tangent height.

parameters are obtained with a vertical resolution of 240 m from the surface up to 25-30 km. Since the aim of this study is the comparison with the PRO observations from PAZ, these parameters are transformed to the "RO observing frame", as is defined below.

In brief, radio occultation observations consist of a Low Earth Orbiter (LEO) tracking a Global Navigation Satellite System (GNSS) emitted signal while it is occulting behind the Earth horizon (e.g. Kursinski et al., 1997; Hajj et al., 2002). This results in the electromagnetic waves from GNSS crossing the different layers of the atmosphere tangentially with respect to Earth's surface, what is commonly known as a limb sounding observation. One implication of this kind of measurement is that rays cross a long portion of the atmosphere, becoming longer as rays approach the surface. In fact, when rays penetrate below 20 km (region where clouds are expected), their traveled distance can be as large as ~ 800 km. In the particular case of PRO, this

90

has been discussed in Turk et al. (2021). Therefore, direct comparisons between the nadir-looking radar obtained parameters with measurements from RO does not provide relevant information in terms of understanding PRO observations.

The approach followed in this study has been to re-map the Cloudsat observed and retrieved parameters into the RO geometry. This is accomplished by using a set of actual RO rays and ~~move and rotate~~ moving and rotating them in order to place them overlaid to the curtain-like Cloudsat observations. RO rays often suffer from a drift as the occultation advances (e.g. the collection of rays do not form a perfectly vertical plane) due to the relative movement of the GNSS satellite and the LEO. However, for this study, the RO rays are collapsed into the Cloudsat vertical plane. Each Cloudsat orbit is split into 1200 km segments (resulting in approximately 29 segments per orbit), and the RO rays are placed in the middle of each of these segments. The first segment of each orbit is randomly displaced to ensure an even sampling of the Earth. After that, Cloudsat observed and derived parameters are interpolated into the RO rays. See Fig. 1-(a and b) for an example of the procedure.

This approach permits the consideration of two relevant things. The first is that one can see the actual extent, and therefore the influence area, of the cloud structures as sensed by PRO. The second one is that the ~~actual amount of water content~~ amount of IWC along RO rays can be quantified (e.g. see panel c in Fig. 1). Therefore, the integrated ~~ice water content~~ IWC along these RO rays can be compared with the PAZ PRO $\Delta\Phi$ observations. Each RO ray is identified by the height of its lowest point along the ray (i.e. height of what is called the "tangent point"), so the integrated quantities are expressed as function of such height.

Such an exercise is repeated for all Cloudsat orbits between 2009 and 2013, resulting in 342,109 artificial RO observations. For each of these artificial ROs, the following parameters are stored:

- Location and UTC time of each artificial RO observation. The location is determined by the latitude and longitude of the tangent point that has an altitude of 5 km. The UTC time is the one corresponding to the Cloudsat observation.

- The integrated IWC along each ray (as a function of tangent height), and the maximum IWC encountered along each ray (e.g. Fig. 1-(c and e)).

- The distance each ray traveled within the influence of non-zero water content (e.g. Fig. 1-(d)).

- Additionally, vertical profiles of some thermodynamic parameters at the location of each artificial RO, like the temperature, pressure and specific humidity, are obtained from the ECMWF auxiliary files.

The resulting data are called hereafter the Cloudsat-RO database. Since the focus will be only on the IWC, each Cloudsat-RO event is truncated at the freezing level to avoid major contributions from liquid phase precipitation. For this study, the effect of mixed-phase precipitation is not taken into account.

2.1 Statistics

Given that Cloudsat is orbiting on a polar orbit similar to that of PAZ satellite, and that RO rays are obtained from real RO events, the statistics gathered from the artificial collocation exercise should resemble the reality observed by PAZ. Furthermore, the integrated parameters along the RO rays mimic the behavior of $\Delta\Phi$ observations, also obtained by PAZ as function of the
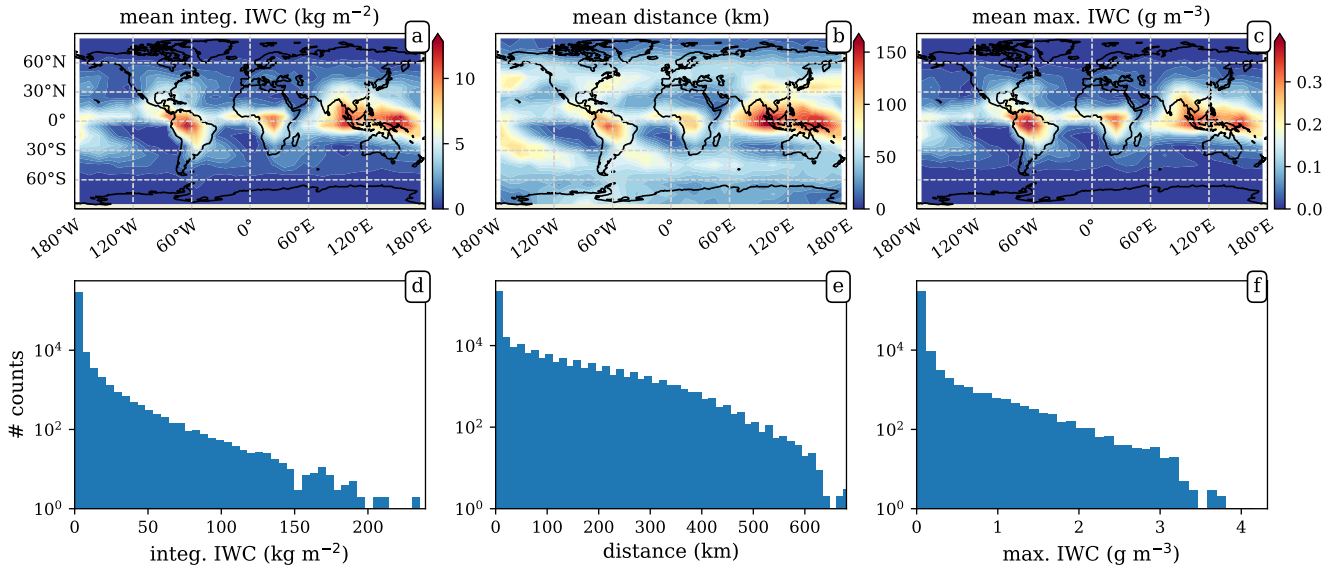
Figure 2. Statistics of the Cloudsat-RO database corresponding to the rays whose tangent height is 9 km. Panels (a), (b) and (c) show the mean value climatology for the along-ray integrated IWC, distance (i.e. distance traveled by each ray within the influence of positive IWC), and maximum IWC encountered along the ray, respectively. The used grid is 10×10 deg. Panels (d), (e), and (f) correspond to the histograms for the total values for the same integrated IWC, distance, and maximum IWC as in the first row. IWC source is the DARDAR retrieval product.

tangent height. Therefore, analysis of the statistics of the artificial Cloudsat-ROs provides us with valuable information in order to understand the PAZ observations.

Figure 2 shows statistics of the along-ray integrated IWC, distance (here defined as the distance traveled by each ray within the influence of positive IWC), and maximum IWC encountered along each ray, obtained from the Cloudsat-RO database using the DARDAR product, corresponding to the rays whose tangent height is 9 km. The first thing to observe is the large values for the along-ray integrated IWC (e.g. Fig 2-d, with values up to 250 kg m^{-2}). This is due to the long distances that rays travel through IWC. In this geometry, the distance relates more to the size of the storms being observed, as opposed to the vertical water path which relates stronger to their intensity. However, the broad range of distances (see Fig 2-e), reveals the ambiguity of PRO, i.e. it cannot distinguish between the effects of intensity of the storm (or amount of water content) and the distance within the influence of such water content (see Eq. 1).

The spatial/geographical patterns are also relevant. Higher concentrations of IWC at 9 km occur in the tropics (as expected), specially over land (south America and central Africa) and around the West Pacific warm pool. Regarding the distance, large values also appear over the mid- and high- latitude oceans. This results agree well with known patters and previous characterization of storm features, such as in Liu and Zipser (2015), meaning that the RO geometry does not pose a problem in obtaining

these global properties of heavy precipitation systems. Therefore, this database of IWC in RO geometry is well suited to both help understand the features observed in the PAZ $\Delta\Phi$ and relate them to realistic precipitating systems.

For this study, the DARDAR V3 retrieval has been used as a reference for the cross-comparison with $\Delta\Phi$. The choice has been made taking into account the assumptions in the IWC retrieval of both DARDAR and 2B-CWC-RO. DARDAR V3 has

145 been recently improved with ~~a lot of~~ in-situ observations to help constrain the particle size distributions (Cazenave et al., 2019). A comparison between the integrated IWC from a Cloudsat-RO generated from DARDAR V3 and 2B-CWC-RO products is shown in Figure A1. The results shown hereafter will refer to those obtained using the Cloudsat-RO generated from DARDAR V3.

3 Relationship between PAZ $\Delta\Phi$ and Cloudsat ice water content

150 As it has been discussed in the introduction, both K_{dp} and WC are affected by the third moment of the $N(D)$. Therefore, a relationship between the two is expected. ~~Being~~ Since the PRO observable ~~,~~ ($\Delta\Phi$~~,~~) is an integral measurement, the ~~corresponding quantity to compare with would be the integrated WC~~ integrated IWC along the same ray where $\Delta\Phi$ has been measured would be the most suitable quantity to be compared with. However, the PAZ satellite is in an 6AM/6PM orbit optimized for its primary sensor, which results in few crossover measurements with the GPM and CloudSat radars. Therefore, the comparison is

155 performed statistically with the Cloudsat-RO database.

For the $\Delta\Phi$ observations, the whole PAZ mission is used. That is, 189,487 $\Delta\Phi$ profiles between May 10th 2018 and May 31th 2022. All these profiles have been selected so they have passed the initial quality controls and calibration ~~(e.g. Padullés et al., 2020)~~ (Padullés et al., 2020). PAZ $\Delta\Phi$ data are available from https://paz.ice.csic.es/.

The noise of the individual $\Delta\Phi$ observations is thoroughly assessed in Padullés et al. (2020). The noise is normally distributed

160 around 0 mm (for the events with no clouds nor precipitation) with a standard deviation that ranges from 1.5-2 mm in the lowest tangent heights (e.g. $\sim$2km, where the signal to noise ratio of the observations is low) to 0.5 mm above 10 km. The major source of uncertainty for the IWC are the retrieval assumptions, and it has been briefly discussed in Appendix A.

Figure 3 shows the comparison of the mean along-ray integrated IWC with the mean $\Delta\Phi$, as a function of latitude, corresponding to a tangent height of 7 km. It can be seen how the two quantities agree remarkably well when the whole datasets are considered (panel a). The agreement is specially good over ocean (panel b). In the tropics, the shape of both the along-ray integrated IWC and $\Delta\Phi$ capture very well the global precipitation signature of the Inter-Tropical Convergence Zone (ITCZ) (e.g. Marshall et al., 2014; Schneider et al., 2014). Over land (panel c), ~~some features are still recognizable, but the general agreement is not as good as over ocean~~ the agreement is also good despite some small deviations between both quantities around the equator.

170 On a map, the gridded mean (or climatology) of $\Delta\Phi$ can be seen in Figure 4. Panel (a) corresponds to the mean $\Delta\Phi$ at a tangent height of 7 km, and panel (b) at a tangent height of 9 km. The latter can be compared with ~~Fig.~~ Figure 2-a to investigate whether the spatial patterns are equivalent or not. In order to quantify the spatial relationship between the two (e.g. PAZ $\Delta\Phi$ and Cloudsat-RO ~~WC~~ IWC), the mean ~~climatologies~~ of both quantities are computed on the same grid. The chosen grid is
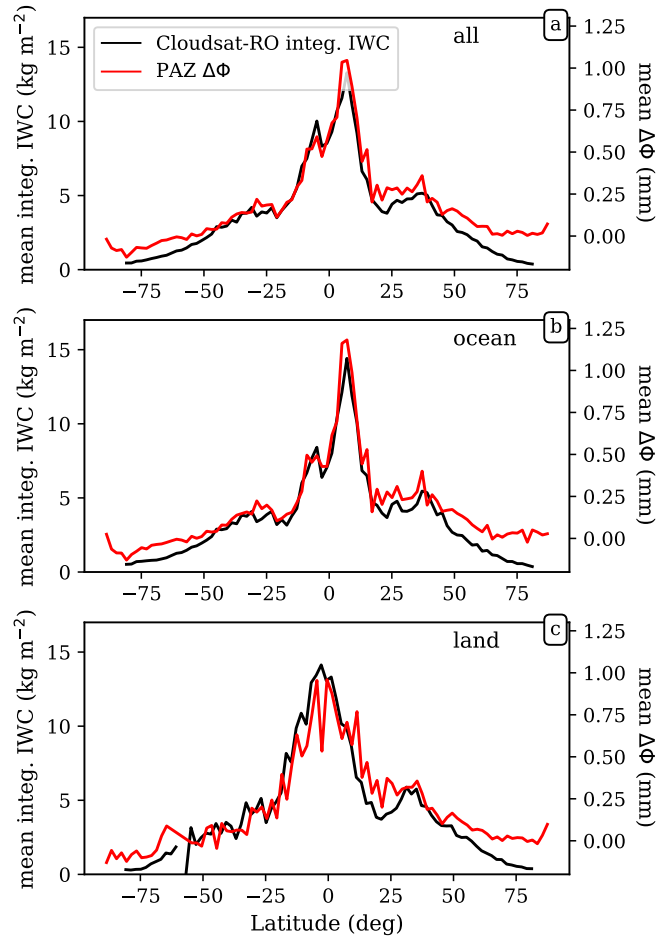
Figure 3. Mean values of integrated IWC (left axes) from the Cloudsat-RO dataset, and mean values of observed $\Delta\Phi$ from PAZ (right axes), as a function of latitude, for all data (a), ocean (b) and land (c). Data correspond to tangent heights of ~~8~~ 7 km. The mean values are computed for every 2 deg latitude bands.

~~12~~15×~~12~~15 deg, so that spatial patterns of precipitation arise and there are enough PAZ observations to achieve significant

175   statistics. The values for the mean ~~climatologies~~ of PAZ $\Delta\Phi$ and integrated Cloudsat-RO IWC obtained at the same grid cells are compared against each other (~~Figure 4-c~~e.g. Figure 5-a). For the case of data corresponding to a tangent height of 9 km, the relationship follows a linear trend. The Pearsons correlation coefficient is ~~0.9~~0.84 (e.g, r^2 = ~~0.81~~0.7) therefore exhibiting a robust relationship.

The correlation coefficient for the spatial relationship between the mean PAZ $\Delta\Phi$ and mean integrated Cloudsat-RO ~~WC~~

180   IWC is computed for heights between 2 and 17 km.

In addition to the mean, the ~~climatologies for~~ 80th and 90th percentiles of both datasets are also computed at the same grid cells. That is, for each grid cell, the distribution for $\Delta\Phi$ and for the Cloudsat-RO integrated IWC is represented, and the 80th
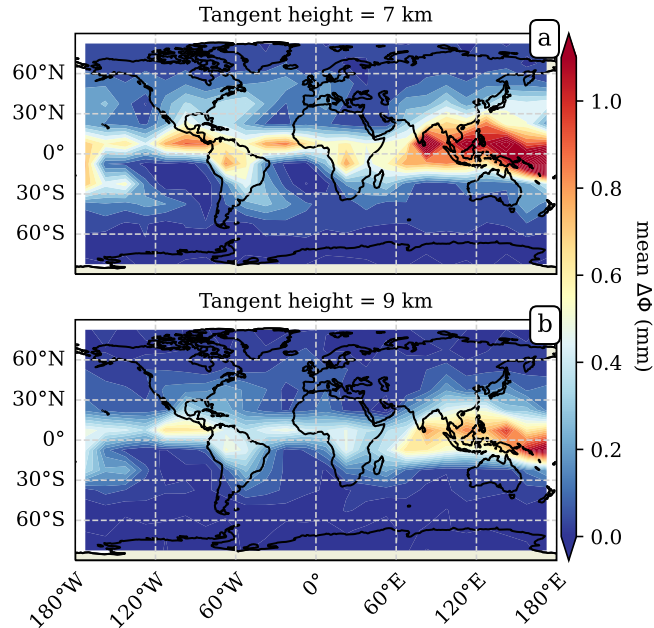
Figure 4. Global climatology maps for the mean PAZ $\Delta\Phi$ observations corresponding to a tangent height of 7 km (panel a) and 9 km (panel b). The grid size where the means are computed is ~~12~~15×~~12~~15 deg. ~~Panel (c) shows the scatter plot of the mean climatologies of Cloudsat-RO integrated WC vs the PAZ $\Delta\Phi$ obtained at the same grid cell, for the data corresponding to a tangent height of 9 km. Therefore, it is the comparison between panel (b) in this figure and Figure 2-a.~~

and 90th percentiles ~~are also computed~~of such distributions are computed. This results in a climatology for the 80th and 90th percentiles of $\Delta\Phi$ and Cloudsat-RO integrated IWC. The approach is shown for two grid cells in Figure 5-b,c. The comparison

185 between the 80th and 90th percentiles climatologies of $\Delta\Phi$ and Cloudsat-RO integrated IWC is performed in order to check if the relationships stands at the higher ends of the distributions. That is, to check whether there is a good agreement between $\Delta\Phi$ and integrated Cloudsat-RO IWC for the whole distribution (and not only for the mean). The results are shown in Figure 6.

Along with the correlation coefficient, the ratio between the ~~mean~~ PAZ $\Delta\Phi$ ~~and mean integrated~~ mean climatology and the Cloudsat-RO ~~IWC~~integrated IWC mean climatology (i.e. ratio = $\Delta\Phi$/IWC) is also computed at the same heights ~~and~~ as the

190 correlation coefficients and is shown in Figure 7. ~~The values for the first rows of Figures 6 and 7 are summarized in Table ??.~~ It is computed from the linear fit between the mean PAZ $\Delta\Phi$ and mean Cloudsat-RO integrated IWC at different cells (e.g. see Figure 5-a, where we assume that the intercept is zero).

3.1 Correlations

The correlation coefficients in Figure 6 quantify the agreement between the spatial or geographical patterns of the two datasets.

195 High correlations can be understood as the two datasets observing the same kind of precipitation structures. One thing to note
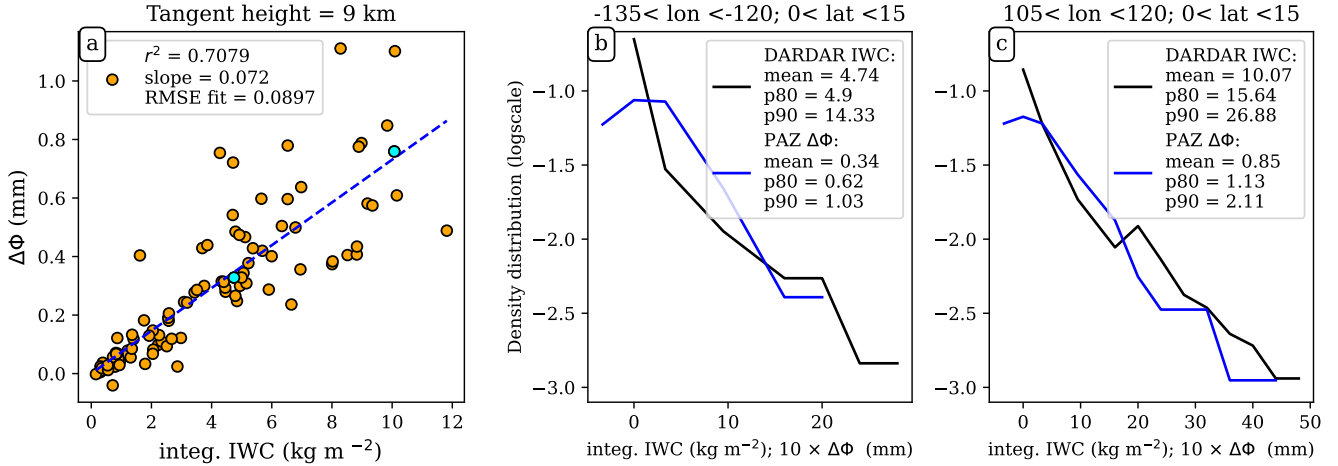
Figure 5. Panel (a) shows the scatter plot of the mean climatologies of Cloudsat-RO integrated IWC vs the PAZ ΔΦ obtained at the same grid cell, for the data corresponding to a tangent height of 9 km and over tropical ocean. Therefore, it is the comparison between the tropical ocean cells in Figure 4-b and Figure 2-a. Panels (b) and (c) show the distribution of Cloudsat-RO integrated IWC (black) and PAZ ΔΦ (blue) for two different grid cells at a tangent height of 9 km. The grid cells correspond to the two cyan points in panel (a) and its location is identified in the panel title with the corresponding longitude and latitude ranges.

before digging deeper into the results is that the correlation coefficient is computed assuming a linear relationship between the two quantities.

The results, in general (e.g. Figure 6 - first row, and Table ?? - first column), show a very high correlation coefficient (i.e. cc>0.8) among most of the considered heights. The correlation is particularly high over the oceans, although over land the
200   agreement is also good. This is true for the three statistics being considered, the mean climatology, and the climatologies for the 80th and 90th percentile of the distributions. However, the correlation coefficient corresponding to the mean tends to be slightly higher than the other two.

When the data are split in different regions (e.g. tropics vs extra-tropics), more detailed features can be explored. The first relevant one is the fact that the correlation coefficient in the tropics (Figure 6 - second column) is higher for a wider range
205   of heights than for the extra-tropical cases (Figure 6 - third and fourth columns). Also, it can be seen how for heights below ~4 km, the correlation in the tropics drops due to the fact that the profiles have been truncated below the freezing level, and therefore there are almost no data below ~4 km. The second relevant feature is that the correlation for the climatologies of the 80th and 90th percentiles are lower outside the tropics. Finally, one must note that the panel corresponding to land in the southern hemisphere (70S-30S) is contributed by a relatively small amount of data points, hence exhibiting a large dispersion
210   of the correlation coefficients among different heights.

3.2   Ratios
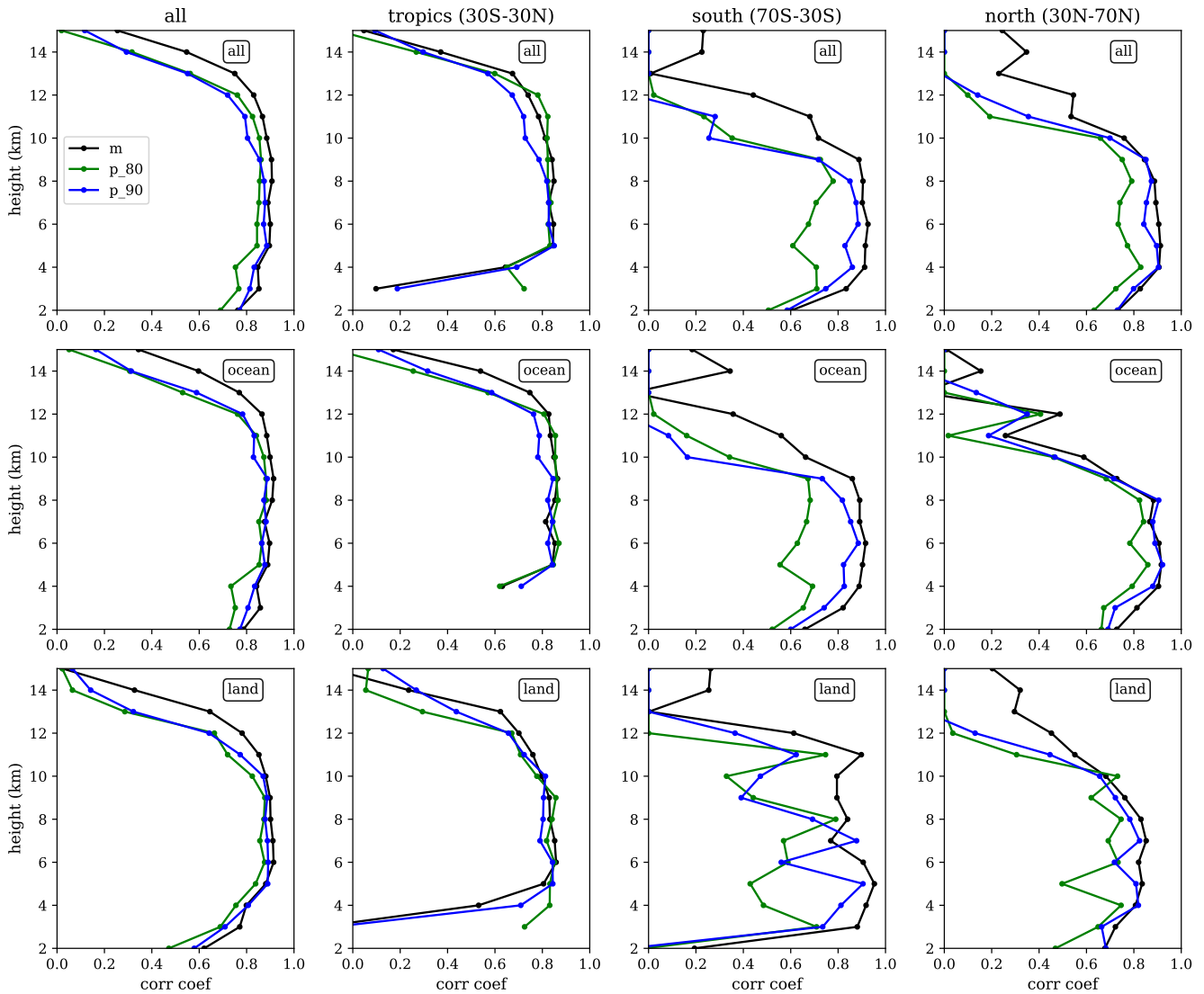
Figure 6. Correlation coefficients between PAZ $\Delta\Phi$ and Cloudsat-RO IWC, as a function of height (y-axis), for different areas across the globe (all globe, tropics, southern extra-tropics, and northern extra-tropics), and different surfaces (all, ocean, land). The black lines correspond to the mean climatologies, the green lines to the 80th percentile and the ~~red~~ blue lines to the 90th percentile climatology.

~~In addition of the correlation coefficient, the~~ The ratio between the mean climatologies of PAZ $\Delta\Phi$ and Cloudsat-RO integrated IWC ~~(i.e. ratio = $\Delta\Phi$/IWC) is computed for the same heights and regions as in Figure 6. Such a ratio~~ provides an empirical relationship between the two quantities and it is shown in Figure 7 (black line). Furthermore, the uncertainty of such ratio (e.g. ~~the standard deviation around the mean value~~ defined here as the root mean squared error around the linear fit) is obtained at each height when performing the linear ~~fit between the~~ regression between the mean climatologies (e.g. as shown in Figure ~~4-c~~ 5-a).
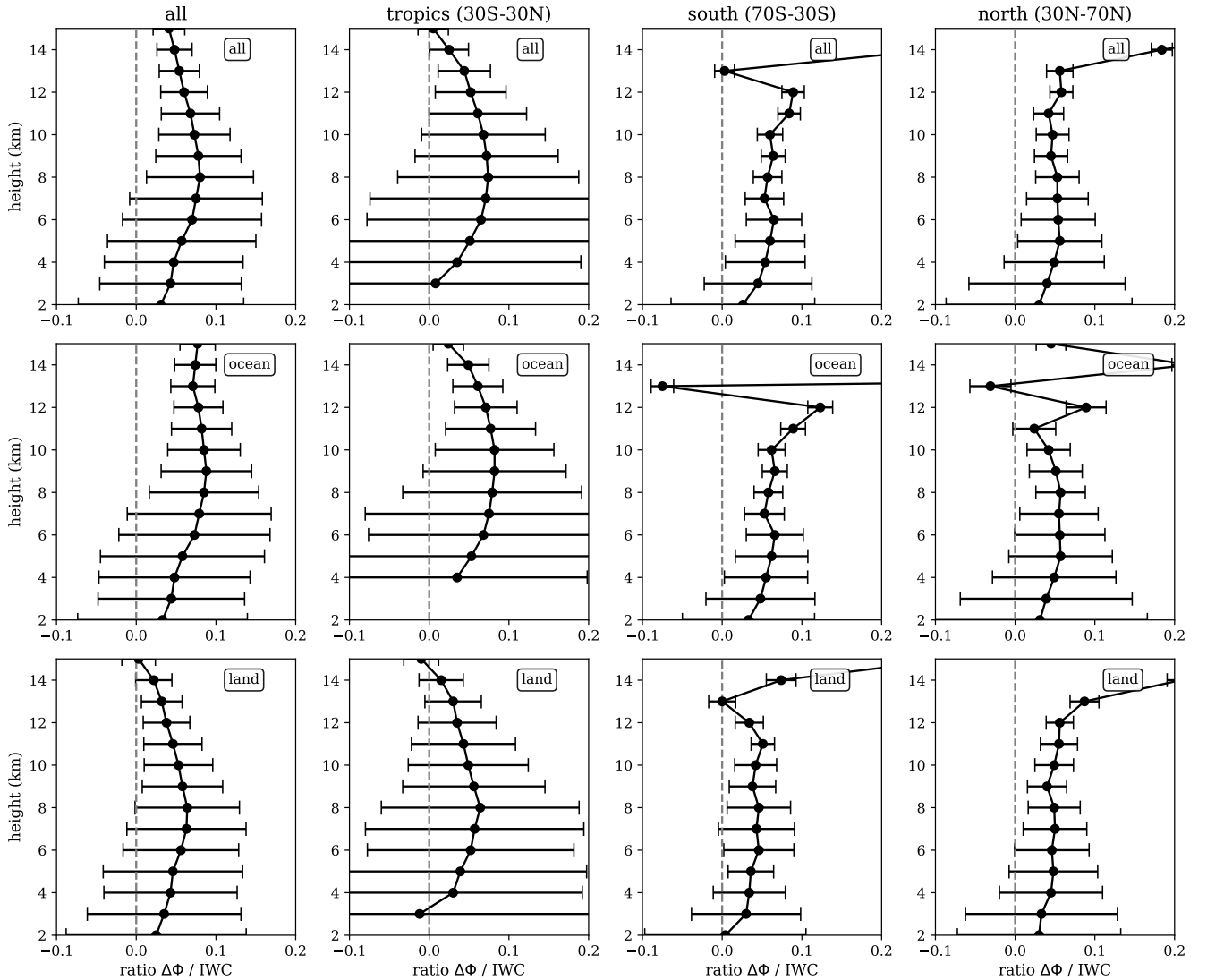
Figure 7. Ratio between PAZ $\Delta\Phi$ ~~mean climatology~~ and Cloudsat-RO ~~integ.~~ IWC ~~mean climatology~~, as a function of height (y-axis), for different areas across the globe (all globe, tropics, southern extra-tropics, and northern extra-tropics), and different surfaces (all, ocean, land). The ~~black lines correspond to the mean climatologies, the green lines to the 80th percentile and the red lines to the 90th percentile climatology. The~~ x-axis errorbars show the ~~standard deviation (1σ) uncertainty~~ root mean squared error around the ~~mean~~ fit from which we obtain the ratio (e~~. The corresponding standard error is not shown, as it is one order of magnitude lower than~~g. see Figure ~~σ~~5).

The ratio is considered meaningful in the heights and regions where the correlation coefficient is high (e.g. cc > 0.8). The values obtained for the ratio of the mean climatologies in such regions and heights ranges from 0.03-0.09 mm kg^{-1} m^2. It can be seen how it has a trend with height~~and it exhibits differences at the different percentiles~~. In general, the ratio tends to

220 maximize at around 8/10km in the tropics, and at a lower heights in the extra-tropics. ~~Furthermore, the ratio corresponding to the 80th and 90th percentile is smaller compared to the one corresponding to the mean climatology, in most heights and all regions.~~

~~Values for the correlation coefficient and ratio between IWC and $\Delta\Phi$ (top and bottom value in each cell, respectively), for different statistics (first column), different regions (second column) and different heights (first row). Data corresponds to the~~
225 ~~whole globe. Values in bold highlight correlation coefficients higher than 0.8.height (km) 3 4 5 6 7 8 9 10 11 12 13 14 **0.85 0.85 0.9 0.9 0.89 0.91 0.9 0.88 0.87 0.83** 0.75 0.55 0.043 0.047 0.057 0.07 0.075 0.08 0.078 0.073 0.068 0.06 0.054 0.048 **0.86 0.84 0.89 0.9 0.88 0.91 0.91 0.9 0.88 0.86** 0.77 0.6 0.044 0.048 0.058 0.073 0.079 0.085 0.088 0.085 0.082 0.078 0.071 0.074 0.77 0.8 **0.88 0.91 0.91 0.9 0.9 0.88 0.85** 0.78 0.64 0.33 0.035 0.043 0.046 0.056 0.063 0.064 0.058 0.053 0.046 0.038 0.032 0.022 0.77 0.75 **0.84 0.84 0.85 0.86 0.86 0.85 0.82** 0.76 0.56 0.32 0.033 0.04 0.041 0.056 0.068 0.054 0.051 0.045 0.039 0.039~~
230 ~~0.036 0.035 0.75 0.73 **0.85 0.86 0.85 0.88 0.88 0.87 0.84** 0.76 0.53 0.31 0.034 0.038 0.044 0.064 0.076 0.063 0.06 0.052 0.046 0.046 0.039 0.041 0.69 0.76 **0.84 0.88 0.86 0.87 0.88 0.82** 0.72 0.66 0.29 0.06 0.025 0.04 0.035 0.042 0.055 0.045 0.038 0.037 0.028 0.032 0.019 0.009 **0.81 0.83 0.88 0.87 0.88 0.87 0.86 0.8** 0.79 0.72 0.55 0.29 0.03 0.033 0.044 0.054 0.064 0.058 0.051 0.046 0.037 0.027 0.021 0.017 **0.81 0.83 0.88 0.86 0.88 0.87 0.89 0.83 0.83** 0.78 0.59 0.31 0.031 0.033 0.044 0.057 0.068 0.062 0.062 0.055 0.047 0.037 0.028 0.022 0.71 **0.81 0.89 0.89 0.89 0.88 0.89 0.87** 0.77 0.64 0.32 0.14 0.024 0.03 0.041 0.042~~
235 ~~0.055 0.051 0.038 0.032 0.024 0.015 0.01 0.009~~

4 Forward scattering simulations of ice and snow

The correlation coefficients obtained in Sect. 3.1 indicate a robust relationship between $\Delta\Phi$ and integrated IWC, especially over tropical ocean. However, the meaning of the ratio between $\Delta\Phi$ and integrated IWC depend on more factors. The aim of this section is to determine whether the ratios in Sect. 3.2 are physically meaningful or not. That is, to determine if the ratios
240 are compatible with the characteristics of hydrometeors that are known to be present in clouds.

For this, the idea is to compute the K_{dp} - IWC relationship for a series of different hydrometeors and ice particle habits. This relationship can then be compared with the ratios in Figure 7~~and in Table ??~~. To perform such comparison, first, the scattering amplitude matrix $\mathbf{S}$ is computed for a set of different single hydrometeors and ice particle habits. Then, a set of particle size distributions from one week of Cloudsat observations are used to generate the corresponding K_{dp} and IWC using Eqs. 2 and
245 3. Note that for this study, only ~~single particle~~ single-particle scattering is considered.

4.1 Hydrometeors and ice particle habits

The forward scattering simulations used for this study have been done using Rayleigh approximation. This formulation assumes that the particles can be approximated as oblate spheroids, with a certain axis ratio and effective density. The list of hydrometeors and ice particle habits that have been used are pristine ice crystals, aggregates of pristine ice, and wet snow.
250 The adequacy of using Rayleigh approximations is justified by the long wavelength of GNSS signals, i.e. $\sim$190.3 mm, much larger than the typical size of frozen hydrometeors. For Rayleight approximations, the formulations in Ryzhkov et al. (2011)

and in Bringi and Chandrasekar (2001) have been followed. That is, the forward scattering amplitude co-polar components are computed using:

$$S_{\mathrm{hh,vv}} = \frac{\pi^2 D^3}{6\lambda^2} \frac{1}{L_{\mathrm{hh,vv}} + \dfrac{1}{\epsilon - 1}} \tag{4}$$

255   where ϵ is the dielectric constant, and $L_{\mathrm{hh,vv}}$ are the shape parameters:

$$L_{\mathrm{hh}} = \frac{1+f^2}{f^2}\left(1 - \frac{\arctan(f)}{f}\right), \quad f = \sqrt{\frac{1}{ar^2} - 1} \tag{5}$$

$$L_{\mathrm{vv}} = \frac{1 + L_{\mathrm{hh}}}{2} \tag{6}$$

where ar is the axis ratio of the particle. For the dielectric constant, the Maxwell-Garnett formula is used in order to account
260   for the effective density of the particles as mixtures of ice, air, and water (Maxwell Garnett, 1904).

For some pristine ice crystals and aggregates, a comparison using the Discrete Dipole Approximation (DDA, Draine and Flatau, 1994) has been performed and compared with the Rayleigh results. The simulations have been performed using exact shape particles from Liu (2008), and the computation for aggregates follows the methodology in Leinonen and Moisseev (2015). The results (not shown) show good agreement with the Rayleigh approximations.

265   Below there are the specific details for each of the hydrometeors and habits used in this study.

4.1.1 Pristine ice crystals

The simplest type of particles used in this study are pristine ice dendrites and thick plates. For the Rayleigh computation, the density of solid ice is used, and the values in Ryzhkov et al. (2011, Table 1) are used for the axis ratio. A fully horizontal orientation of the particles is assumed.

270   ### 4.1.2 Aggregates

For more complex shapes, we use aggregates of pristine ice particles. For the Rayleigh approximation, an spheroid of air filled with portions of ice is used, following Ryzhkov et al. (2011) and taking different values for the effective density and axis ratio. The computation is performed for effective densities ranging from 0.1 to 0.9 $\mathrm{g\,cm}^{-3}$, and axis ratios ranging from 0.2 to 0.9. Note that using an effective density of 0.9 means that the spheroid is filled with ice, approaching a pristine ice particle. The
275   results using the Rayleigh method for fixed densities and fixed axis ratios for the whole range of equivalent diameters are called dry aggregates.

4.1.3 Wet snow

Finally, wet snow aims to represent frozen particles at the initial stages of melting. For this, the same spheroids as in the previous subsection are used, but for this case a mass faction of liquid water of a 10% of the total mass is used, in addition to

280   pure ice and air, to compute ϵ. The presence of water in the particle enhances ϵ which in turn increases the K_{dp} with respect to the dry aggregates with same parameters (of equivalent density and ar).

4.2   Orientation angle distribution

The results for pristine ice, aggregates and wet snow are computed using single particle scattering and forcing the different particles to be horizontally oriented. This is unlikely to be the case in real clouds and storms, where the orientation of these

285   particles is more complex. To account for different orientation angles, we assume a Gaussian distribution of tilt (or canting) angles centered at $0°$ (hence mean angle $\beta = 0°$) with a certain standard deviation σ. This implies that varying σ we can range from total horizontal orientation ($\sigma = 0°$) to completely random orientation (large σ). To keep the computations simple, we can use the horizontal orientation values and multiply them by a factor that accounts for such canting (Oguchi, 1983):

$$K_{\mathrm{dp}}^{\sigma} = \frac{1 + e^{-2\sigma^2}\cos(2\beta)}{2}e^{-2\sigma^2}\,K_{\mathrm{dp}}^{\sigma=0} \tag{7}$$

290 ## 4.3   Simulations results

Using one week of Cloudsat retrieved $N(D)$ at different heights above the freezing level, the IWC and K_{dp} are computed using the same particle type. This results in a set of K_{dp} vs IWC relationships for different hydrometeors or ice particle habits, and different properties such as effective density (ρ) and axis ratios. In addition, for each combination of particle type, ρ and ar, the corresponding result at different distributions of tilt angles are performed. Figure 8 it is shown the variability of the

295   K_{dp} vs IWC relationship, for dry aggregates (and wet snow), when one of the properties is varied (e.g.distribution of tilt angles -panel a-, effective density -panel b-, axis ratio -panel c-, and effective density for wet snow -panel d-).

The ratios between the K_{dp} and IWC for a subset of particles and different properties are shown in Table 1. The ratios with a value within the range [0.03 - 0.09] are highlighted in bold. These are the values agreeing with the reported ratios between $\Delta\Phi$ and integrated IWC in Sect. 3.

300   In ~~this~~ these results, it can be seen how for more pristine and thin particles, certain canting angle is required (e.g. fully horizontal orientation is overestimating the observed K_{dp}), whereas for more complex particles, these are required to stay more horizontally oriented to better match the actual data. It can also be observed that very low density particles with high axis ratios (i.e. approaching empty spheres) alone cannot explain the observations.

To further validate observations and results obtained in Section 3 and allow for a more equivalent comparison between the

305   results, a simple exercise is performed. It consists ~~on~~ of computing the integrated IWC and $\Delta\Phi$ using the simulations just described, and ~~to proceed~~ proceeding with the same procedure followed in Section 3 in order to obtain the same relationships. That is, to compute the mean climatological values at the same grid bins and heights, but in this case, for the simulated $\Delta\Phi$ values. The obtained values for $\Delta\Phi$ at all grid bins and heights are shown as a function of the corresponding integrated IWC at the same grid bins and heights in Figure 9 -top row-. This is done for dry aggregates with a different combination of ρ and

310   ar, and for different tilt angles distribution. The same approach is used to compare the simulated $\Delta\Phi$ with the observed one, as shown in Figure 9 -bottom row-.

Table 1. Ratio between K_{dp} and IWC for the different hydrometeors shown in Fig. 8, when a certain standard deviation is assumed in the orientation distribution (Gaussian distribution centered at $0°$ and σ) $\sigma = 0°$ represents the scenario where all particles are horizontally oriented, while for large σ all particles would be randomly oriented (see Eq. 7). In bold, the ratios within the range [0.03 - 0.09], in agreement with the observed ratios in Fig. 6~~and Table ??~~.

	standard deviation of the Gaussian distribution of orientations, σ (°)								
	0	10	20	30	40	50	60	70	80
wet snow 0.9 ar 0.2	0.797	0.728	0.557	0.363	0.207	0.106	**0.049**	0.021	<0.015
crystal thick plate	0.607	0.555	0.424	0.277	0.158	**0.081**	**0.038**	0.016	<0.015
dry agg 0.9 ar 0.2	0.556	0.507	0.388	0.253	0.144	**0.074**	**0.034**	0.015	<0.015
wet snow 0.5 ar 0.2	0.414	0.378	0.289	0.189	0.108	**0.055**	0.026	<0.015	<0.015
agg plate	0.388	0.354	0.271	0.177	0.101	**0.052**	0.024	<0.015	<0.015
dry agg 0.5 ar 0.2	0.301	0.275	0.21	0.137	**0.078**	**0.04**	0.019	<0.015	<0.015
agg dendrite	0.288	0.263	0.201	0.131	**0.075**	**0.038**	0.018	<0.015	<0.015
crystal dendrite	0.216	0.197	0.151	0.098	**0.056**	0.029	<0.015	<0.015	<0.015
wet snow 0.9 ar 0.8	0.146	0.133	0.102	**0.067**	**0.038**	0.019	<0.015	<0.015	<0.015
wet snow 0.2 ar 0.2	0.131	0.12	0.092	**0.06**	**0.034**	0.017	<0.015	<0.015	<0.015
dry agg 0.2 ar 0.2	0.12	0.11	**0.084**	**0.055**	**0.031**	0.016	<0.015	<0.015	<0.015
dry agg 0.9 ar 0.8	0.103	0.094	**0.072**	**0.047**	0.027	<0.015	<0.015	<0.015	<0.015
wet snow 0.5 ar 0.8	**0.074**	**0.068**	**0.052**	**0.034**	0.019	<0.015	<0.015	<0.015	<0.015
dry agg 0.5 ar 0.8	**0.054**	**0.049**	**0.038**	0.025	<0.015	<0.015	<0.015	<0.015	<0.015
wet snow 0.2 ar 0.8	0.022	0.02	0.015	<0.015	<0.015	<0.015	<0.015	<0.015	<0.015
dry agg 0.2 ar 0.8	0.02	0.018	<0.015	<0.015	<0.015	<0.015	<0.015	<0.015	<0.015

~~These~~ For simplicity, these results are obtained assuming the same hydrometeor type at all heights for all ~~situation~~situations, which is unrealistic. ~~However, it~~ Similarly, the same effective density has been assumed for each hydrometeor at different sizes, while a more realistic approach would be to assume that the density decreases with particle size. However, these simulations can be used to explain the bulk of the observations, and further assess the effect of considering more or less tilted particles in the simulations in reproducing the observations. Comparing the simulated results with the observations (represented in the top row of Figure 9 as black dashed contour) it can be seen how the bulk observations can be reproduced using dry aggregated particles ~~, of a diverse effective density and axis ratio depending on how tilted they are (e.g., dry aggregate of~~ with a diversity of effective densities and axis ratios depending on the tilt angle distribution. For example, dry aggregates with $\rho = 0.9 \, \mathrm{g\,cm^{-3}}$ and $ar = 0.2$ must have a standard deviation of the tilted angle distribution larger than $50°$ in order to explain the observed relationships~~)~~.
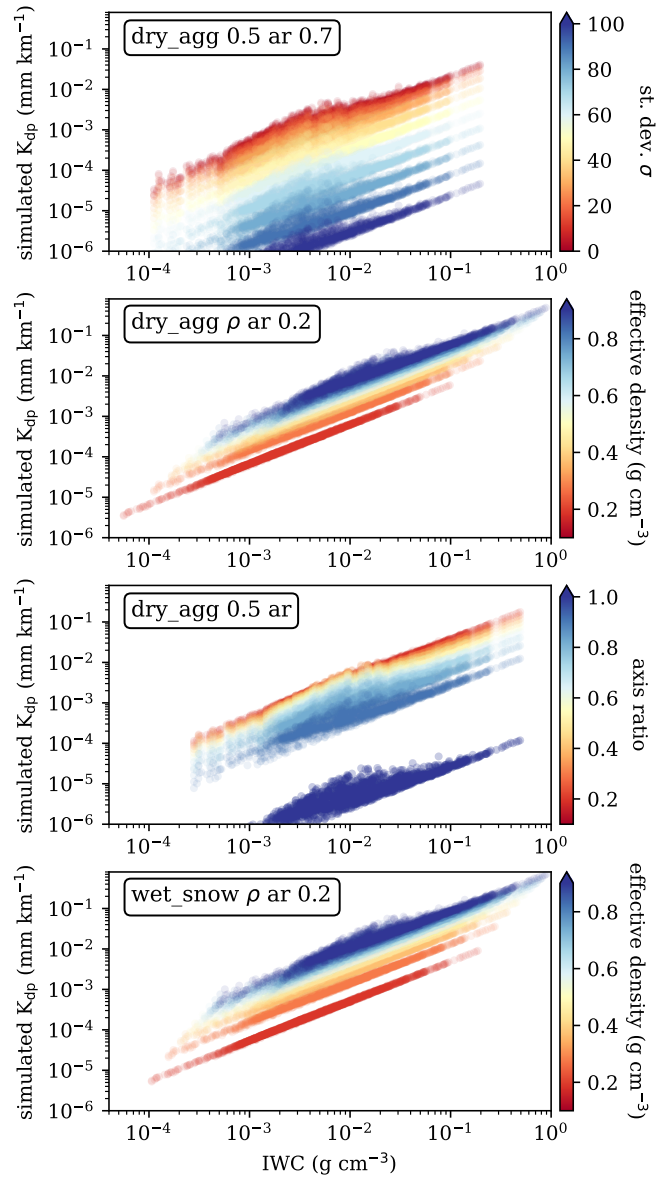
Figure 8. Results of simulated K_{dp} as a function of IWC for dry aggregates (a-b-c), and wet snow (d), varying the standard deviation of the tilt angle distribution (a), the effective density (b), axis ratio (c), and the effective density of wet snow (d).
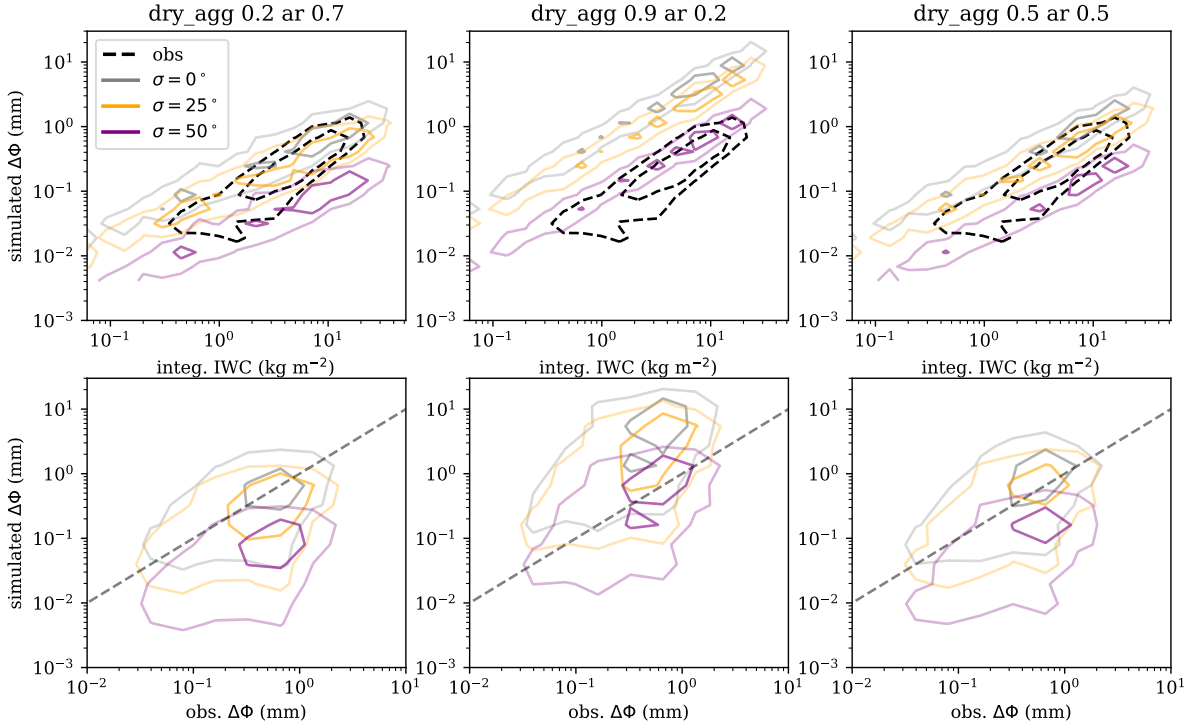
Figure 9. Results of the distributions of simulated $\Delta\Phi$ vs integrated IWC (top row) and vs the observed $\Delta\Phi$ (bottom row) compared at the same grid bins (same approach and same grid bins as in Figure 4) and accounting for all heights. Panel (a) and (d) show the results obtained using a single type of particle at all locations and heights - the dry aggregates with effective density of $0.2\,\mathrm{g\,cm^{-3}}$ and an axis ratio of 0.7. Panels (b) and (e) correspond to results using dry aggregates with effective density of $0.9\,\mathrm{g\,cm^{-3}}$ and an axis ratio of 0.2, and (c) and (f) using dry aggregates with effective density of $0.5\,\mathrm{g\,cm^{-3}}$ and an axis ratio of 0.5. The different colors of the contours correspond ot different standard deviation in the distribution of tilt angles as described in the legend. The dashed contours (in the top row) correspond ot the observed relationships as obtained in Sect. 3. The dashed line (in the bottom row) indicates the perfect 1:1 agreement. The same color inner and outer contours represent the contour containing 30% and 70% of the data, respectively.

5 Summary and discussion

5.1 Observations

The relationship between the PRO observable $\Delta\Phi$ and ice water content has been investigated in a global and statistical (or climatological) way. For this purpose, retrievals from the Cloudsat mission have been used. These have been re-mapped into the RO observation geometry so that comparisons take into account the important features of the observation geometry of PRO. An important one is the long distances that rays traveling from the GNSS satellites to the receivers in Low Earth Orbit spend in the lower layers of the troposphere. Such re-mapping allows an evaluation of the geometry itself. It can be assessed whether a limb-sounding measurement like PRO is able to capture important features of precipitation or not.

The results in Figure 2 show the agreement between the climatology of the along-ray integrated ice water content (and related products such as the distance rays traveled within areas of non-zero ice water content, or the maximum ice water content encountered per ray) with known and previously studied heavy precipitation features (e.g. Liu and Zipser, 2015). This is further confirmed with the results in Figure 3 (showing the mean climatology as function of latitude for water content, solid black line), which agrees very well with the signature of the ITCZ. Therefore, the good climatological agreement enables the use of the Cloudsat-based artificially collocated RO database of along-ray integrated ice water content for understanding the PRO observations of precipitating cloud structures. For this study, only ice water content retrievals are used, and the RO profiles are truncated at the freezing level. The use of ice only retrievals is justified because Cloudsat observations in the liquid region of deep cloud structures (such as those specifically targeted by the ROHP experiment) may be degraded due to the high frequency and penetration issues.

The PRO observable $\Delta\Phi$ is the integrated K_{dp} along each RO ray. Both K_{dp} and water content are affected by the third moment of the $N(D)$, and therefore a relationship between them is to be expected. Such relationship is investigated by evaluating the correlation coefficient between the geographical patterns of the high and low concentrations of $\Delta\Phi$ and along-ray integrated IWC, split in different regions and heights. Overall, correlation coefficients (e.g. Figure 6) are high for the heights where frozen particles are expected (which changes by region, e.g. tropics vs. outside tropics). The correlation coefficients maximize for Tropical oceans.

When the correlation coefficient is evaluated for the higher ends of the distribution (i.e. the climatologies for the 80th and 90th percentiles), similar behavior is observed in the tropics, whereas differences between the mean climatology and the higher percentiles are observed in the mid-latitudes, especially over the southern oceans. This means that the features exhibited in the tail of the distribution of the retrieved IWC in this region are not well captured by PAZ $\Delta\Phi$. One hypothesized explanation could relate to the retrievals within mixed-phase clouds in the Southern Oceans (which are present in the lower heights in these areas), that have posed a longstanding issue for observations (e.g. Mace et al., 2021). Hence, further work must be carried out to assess whether the discrepancies between PAZ $\Delta\Phi$ and Cloudsat-retrieved ice water content in these areas are due to microphysical reasons (e.g. smaller ice particles, lack of preferred orientation, etc.), observational errors, or still unaccounted factors.

The ratio between the mean climatology of $\Delta\Phi$ and Cloudsat-RO integrated IWC aims at quantifying the empirical relationship between both. Results in Figure 7 show the empirical relationship along with its uncertainty, at each height and for different regions. The found ratio lays between 0.03 and 0.09 mm kg^{-1} m^2. The uncertainties show the variation of the ratio around its mean and it shows how, even for mean climatological values, there is a large dispersion that may be explained in part by the non-unique relationships between $\Delta\Phi$ and integrated IWC.

This has been in fact observed in Gong and Wu (2017), where a decrease in the passive microwave polarimetric brightness temperature difference at 166GHz and 89Ghz is seen at very cold brightness temperatures, associated with very deep convective areas. An extreme example of such scenario applied here could be a region of large IWC with totally random oriented particles, where the ratio between $\Delta\Phi$ and IWC would tend to 0 despite having high IWC. This effect would be masked in the mean climatology, but could appear in individual observations. A more detailed study should be conducted to assess these situations, desirably with coincident observations between PRO and radars.

Another interesting feature of the ratio between $\Delta\Phi$ and IWC shown in Figure 7 is that it is in general not constant with height. This could be associated to the presence of different particles at different heights, consistent with particle shape dependence on temperature and supersaturation (e.g. Bailey and Hallett, 2009). Furthermore, differences in the ratio trend with height can be observed between over-ocean and over-land, especially in the tropics, where a decrease in the correlation coefficient is observed at lower heights than for over-ocean. Two main hypothesis could explain the differences: (1) differences in the microphysics over-ocean and over-land, impacting the shape and orientation of the frozen particles; (2) differences owing to different local time observations between PAZ (6am/pm) and Cloudsat (1:30am/pm). The latter would have stronger effect over land, but to discern between the two hypotheses more observations at different orbital planes are needed.

The robust relationships between PRO $\Delta\Phi$ and integrated IWC has an implicit and important implication: it demonstrates the systematic presence of horizontally oriented frozen particles thorough the different vertical cloud layers (above freezing level), globally. This conclusion expands upon results in Defer et al. (2014); Gong and Wu (2017); Zeng et al. (2019), where the presence of horizontally oriented particles was observed globally using the Microwave Analysis and Detection of Rain and Atmospheric Structures (MADRAS) instrument on board the Megha-Tropiques satellite and the Global Precipiation Mission Microwave Imager (GPM-GMI) polarization differences (PD) at 157, 89 and 166 GHz. Thanks to the off-nadir looking instrument, the PD can be related to differential extinction by asymmetric particles. Also, similarly as here with $\Delta\Phi$, using PD from passive microwave radiometers provide a single column measurement, but in the quasi-vertical direction. Here, however, we can include the vertical information lacking to off-nadir looking microwave measurements.

5.2 Simulations

Seeking to assess the feasibility of the results in Section 3, single particle forward scattering simulations have been used to assess whether the relationships obtained between $\Delta\Phi$ and ice water content are reliable, according to the typical types of hydrometeors found in clouds. The assumptions made for the simulations are quite simple, e.g. mostly focused on dry aggregates with a range of ρ, ar and tilt angle distributions.

Using a subset of $N(D)$ and the simulated $\mathbf{S}$, the relationship between IWC and K_{dp} is shown in Figure 8, where a wide diversity of combinations of tilt angle distributions, effective densities and axis ratios ~~is~~ are computed. Many different combinations yield similar results in the relationship K_{dp} vs IWC, revealing the large amount of degrees of freedom in ice particle forward scattering simulations.

The results of the ratio between K_{dp} and IWC for a subset of particles with some combinations of ρ, ar and tilt angle distributions are summarized in Table 1. It is also compared with the results in Section 3.2. The comparison allow us to

corroborate that the observed ratios in the regions with high correlation coefficients can be explained with the simulations using simple approximations, and ~~helps constraining the kind of particles that are likely to be contributing to IWC or not~~could potentially help constraining the plausible distributions of ice crystals that can reproduce the ratios. For example, particles with large axis ratios (e.g. approaching spheres) cannot reproduce the bulk of observed ratios between $\Delta\Phi$ and IWC. Similarly, thin, solid ice particles would need to be oriented with a large dispersion in the tilt angle for the ratios to be consistent with observations.

Statistically comparing the simulated and observed $\Delta\Phi$ and IWC relationship repeating the approach followed in Section 3 but using the simulated K_{dp} (Figure 9), a fairly good agreement is also reached with simple assumptions about the particles and changing the tilt angle distributions. However, the dispersion in Figure 9- bottom row, when comparing simulated with observed gridded mean $\Delta\Phi$ is probably indicating that using the same particle assumptions for all regions and heights is not realistic. A better simulation exercise would be required, e.g. with Numerical Weather Prediction model outputs with detailed information about the hydrometeor species, to further constrain the valid particle shapes and tilt angle distributions that better match the observations (similarly to what is done in Brath et al. (2020)). However, and despite the simplicity, the results obtained here seem compatible with those by Brath et al. (2020). They showed how previously observed relationships between passive microwave brightness temperatures and its polarization differences could be explained accounting for tilted large snow thin plates, or less tilted more complex snow aggregates.

An important note to add is that the results presented here are valid for the chosen IWC retrieval algorithm (in this case, the DARDAR V3), and are therefore dependent on that choice. In particular, the DARDAR V3 algorithm assumes non-spherical ice particle shapes (Delanoë and Hogan, 2010; Cazenave et al., 2019) as opposed to the 2B-CWC-RO algorithm, which uses spherical solid ice particles (Austin et al., 2009). However, none of them takes explicitly into account the orientation of such particles. As can be seen in Appendix A, differences between IWC retrieved in the 2B-CWC-RO product and DARDAR can be large at some heights. This results (not shown) in differences in the computed correlation coefficients at lower heights (i.e. near the freezing level), where the results using DARDAR exhibit larger values for a wider range of heights for most regions. Some differences also appear in the values of the ratios, as can be deduced from Figure A1-panels b and c. As a consequence, the combination of ρ, ar and tilt angle distributions that explain the observed ~~mean~~ ratios would change, but for most ~~regions and heights~~ of the cases considered in this study (i.e. above the freezing level) would remain within ~~the expected values~~equivalent ranges.

6 Conclusions

This study assessed the global relationship between polarimetric radio occultation observable $\Delta\Phi$ and ice water content retrieved by Cloudsat. First of all, the integrated IWC retrievals from Cloudsat have been re-mapped into the RO-like geometry. This has been used to demonstrate that RO-type limb-sounding observations can be used to sense and detect known precipitation features globally.

The global climatology of Cloudsat-retrieved integrated IWC has been compared to the $\Delta\Phi$ climatology from PAZ. It has been shown how the spatial/geographical correlation between the two datasets is high (cc>0.8) for a wide range of heights, ~~and especially good over tropical oceans~~including both ocean and land areas. This means that the IWC concentration patterns are well captured by PRO observations, globally and at different heights. The correlation coefficient maximizes and it is particularly good over tropical oceans for a range of heights ranging from 5 to 12 km.

~~Analysis of the ratio between~~ The ratios between the mean $\Delta\Phi$ and the ~~integrated IWC~~ mean integrated IWC climatologies are found to be within the range 0.03-0.09 mm kg^{-1} m^2. Their analysis yields interesting results as well. First of all, the existence of such relationship between ~~the~~ both quantities implies the systematic presence of horizontally oriented hydrometeors contributing to IWC, globally and at all heights. Second, the dispersion and differences at different heights indicate that indeed different particles have different K_{dp}/IWC ratio.

Furthermore, forward scattering simulations of simple snow aggregates accounting for a range of effective densities, axis ratios, and tilt angles distributions can explain the bulk of the ratios (i.e. the mean climatological values). The simulation framework described here, although being very simple, can easily scale in complexity for arbitrary complex inputs of ice particle habits from, e.g. ~~from~~ Numerical Weather Prediction models, or to account for more realistic assumptions about the effective density.

~~Despite the good agreement~~

Despite the high correlation between the mean values of $\Delta\Phi$ and integrated IWC, further work must be pursued to explore individual simultaneous observations of $\Delta\Phi$ and IWC, and assess when and under which scenarios the relationship holds (i.e. horizontally oriented particles contribute to the IWC) or does not apply (i.e. mostly non oriented ice contributing to IWC). This is enabled by the fact that $\Delta\Phi$ observations inherently provide unique information of the orientation of hydrometeors.

Appendix A: Comparison between DARDAR and 2B-CWC-RO integrated IWC profiles

A comparison of the integrated IWC from the Cloudsat retrieval using the 2B-CWC-RO and DARDAR V3 products has been performed and is shown in Figure A1. The differences in general are shown in panel (a). A more detailed view of the comparison between DARDAR V3 ~~–~~and 2B-CWC-RO integrated IWC at different heights is shown in panel (b), representing the fractional difference between the two datasets. The differences are positive (i.e. DARDAR V3 > 2B-CWC-RO) and larger at lower layers, and shift to negative (i.e. DARDAR V3 < 2B-CWC-RO) at upper layers. A map showing how the differences are distributed on the grid cells used thorough the paper is shown in panel (c) for a tangent height of 6km.

The differences arise from different assumptions regarding the treatment of the Cloudsat observations near the freezing level, the assumptions about the particle size distributions, and DARDAR includes Calipso observations to complement Cloudsat observations ~~(Delanoë and Hogan, 2008, 2010; Cazenave et al., 2019; Austin et al., 2009)~~(Delanoë and Hogan, 2008; Austin et al., 2009; De .

The differences in the integrated IWC would change the results from Section 3. The correlation coefficient exhibit lower values for heights near the freezing level when 2B-CWC-RO is used, and regions over land also exhibit lower correlation coeficient
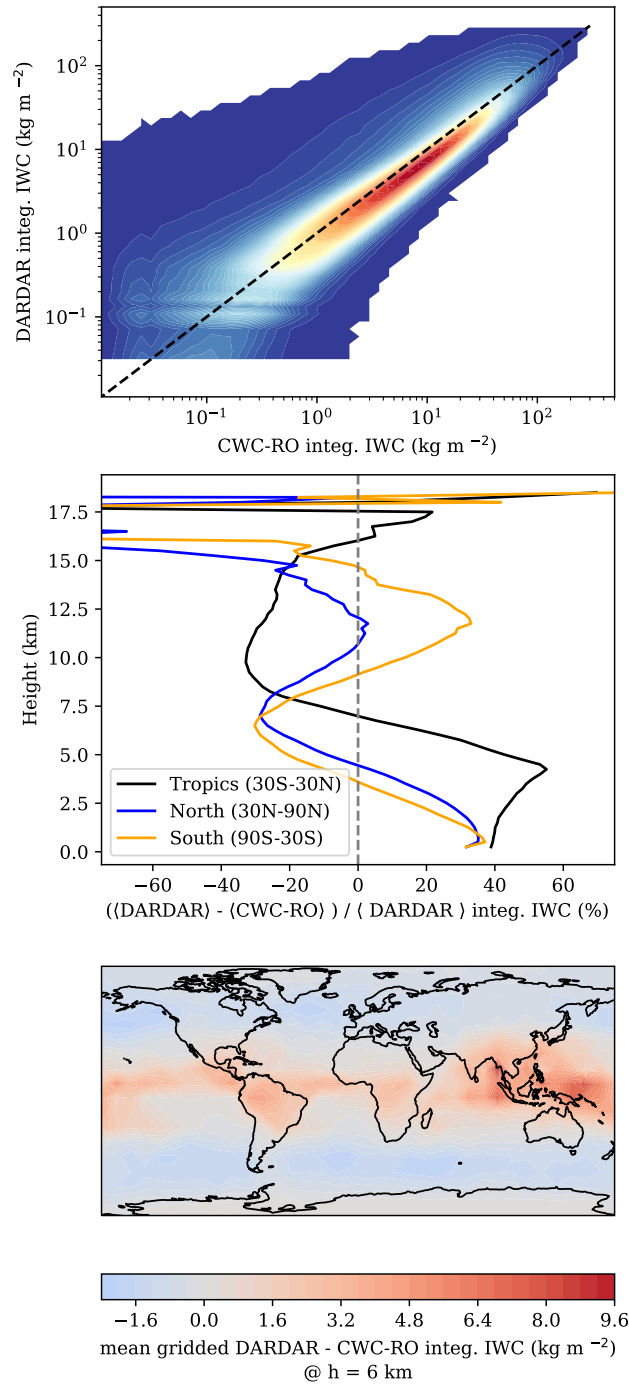
Figure A1. Comparison between the integrated IWC from the Cloudsat retrieval using the 2B-CWC-RO and DARDAR V3. Panel (a) shows the relationship between integrated IWC from the 2B-CWC-RO (x-axis) and DARDAR V3 (y-axis) for all observations regardless of height. Panel (b) shows the fractional difference between the mean DARDAR V3 and 2B-CWC-RO integrated IWC as a function of height, for three different latitudinal bands (see legend). Panel (c) shows the gridded mean DARDAR - 2B-CWC-RO integrated IWC corresponding to a tangent height of 6 km

with 2B-CWC-RO. The ratios between the $\Delta\Phi$ and the integrated IWC change accordingly to the differences between the two IWC ~~product~~products, since $\Delta\Phi$ ~~is the same .~~

465   ~~Comparison between the integrated IWC from the Cloudsat retrieval using the 2B-CWC-RO and DARDAR V3. Panel (a) shows the relationship between integrated IWC from the 2B-CWC-RO (x-axis) and DARDAR V3 (y-axis) for all observations regardless of height. Panel (b) shows the difference DARDAR V3 - 2B-CWC-RO integrated IWC corresponding to different tangent heights as detailed in the legend. Panel (c) shows the gridded mean DARDAR V3 - 2B-CWC-RO integrated IWC corresponding to a tangent height of 6 km.~~ would be the same (e.g. see Figure A1-b).

470   *Data availability.* The datasets used for this work are the following: The PAZ polarimetric Radio Occultation data can be obtained from https://paz.ice.csic.es (last accessed: October 12, 2022). The DARDAR dataset can be obtained from https://www.icare.univ-lille.fr/ (last accesses: October 12, 2022). The Cloudsat 2B-CWC-RO dataset can be obtained from https://www.cloudsat.cira.colostate.edu/ (last accessed: October 12, 2022)

Author contributions. All co-authors have reviewed, discussed, and agreed to the final version of the manuscript. Conceptualization: RP, 475   EC, FJT; Data analysis: RP; Investigation: RP, EC, FJT; Writing – original draft preparation: RP; Writing – review & editing: RP, EC, FJT; Funding acquisition: EC, FJT.

Competing interests. The authors declare no competing interests

Acknowledgements. The authors would like to thank Patrick Eriksson and one anonymous reviewer for their comments and suggestions, which definitely help improve the paper.

480   RP has received funding from the postdoctoral fellowships program Beatriu de Pinós, funded by the Secretary of Universities and Research (Government of Catalonia) and by the Horizon 2020 program of research and innovation of the European Union under the Marie Sklodowska-Curie grant agreement No 801370. This work was also partially supported by the program Unidad de Excelencia María de Maeztu CEX2020-001058-M. The ROHP-PAZ project is part of the ~~Grant~~ Grants RTI2018-099008-B-C22 and PID2021-126436OB-C22 funded by the Spanish Ministry of Science and Innovation MCIN/AEI/10.13039/501100011033 and by "ERDF A way of making Europe" of the "European Union".
485   Part of the investigations are done under the EUMETSAT ROM SAF CDOP4, and are based upon work from CSIC-PTI TELEDETECT members. FJT acknowledges support from NASA under the US Participating Investigator (USPI) program. The work performed by FJT was conducted at the Jet Propulsion Laboratory, California Institute of Technology, under a contract with NASA.

References

Austin, R. T., Heymsfield, A. J., and Stephens, G. L.: Retrieval of ice cloud microphysical parameters using the CloudSat millimeter-wave radar and temperature, Journal of Geophysical Research Atmospheres, 114, 1–19, https://doi.org/10.1029/2008JD010049, 2009.

Bailey, M. and Hallett, J.: A Comprehensive Habit Diagram for Atmospheric Ice Crystals: Confirmation from the Laboratory, AIRS II, and Other Field Studies, Journal of Atmospheric Sciences, 66, 2888–2899, https://doi.org/10.1175/2009JAS2883.1, 2009.

Barlakas, V., Geer, A. J., and Eriksson, P.: Introducing hydrometeor orientation into all-sky microwave and submillimeter assimilation, Atmospheric Measurement Techniques, 14, 3427–3447, https://doi.org/10.5194/amt-14-3427-2021, 2021.

Battaglia, A., Ajewole, M. O., and Simmer, C.: Evaluation of radar multiple scattering effects in Cloudsat configuration, Atmospheric Chemistry and Physics, 7, 1719–1730, https://doi.org/10.5194/acp-7-1719-2007, 2007.

Brath, M., Ekelund, R., Eriksson, P., Lemke, O., and Buehler, S. A.: Microwave and submillimeter wave scattering of oriented ice particles, Atmospheric Measurement Techniques, 13, 2309–2333, https://doi.org/10.5194/amt-13-2309-2020, 2020.

Bringi, V. N. and Chandrasekar, V.: Polarimetric doppler weather radar; principles and applications, Cambridge University Press, Cambridge, 2001.

Bukovčić, P., Ryzhkov, A. V., Zrnić, D. S., and Zhang, G.: Polarimetric radar relations for quantification of snow based on disdrometer data, Journal of Applied Meteorology and Climatology, 57, 103–120, https://doi.org/10.1175/JAMC-D-17-0090.1, 2018.

Cardellach, E., Tomás, S., Oliveras, S., Padullés, R., Rius, A., de la Torre-Juárez, M., Turk, F. J., Ao, C. O., Kursinski, E. R., Schreiner, W. S., Ector, D., and Cucurull, L.: Sensitivity of PAZ LEO Polarimetric GNSS Radio-Occultation Experiment to Precipitation Events, IEEE Transactions on Geoscience and Remote Sensing, 53, 190–206, https://doi.org/10.1109/TGRS.2014.2320309, 2014.

Cardellach, E., Oliveras, S., Rius, A., Tomás, S., Ao, C. O., Franklin, G. W., Iijima, B. A., Kuang, D., Meehan, T. K., Padullés, R., de la Torre-Juárez, M., Turk, F. J., Hunt, D. C., Schreiner, W. S., Sokolovskiy, S. V., Van Hove, T., Weiss, J. P., Yoon, Y., Zeng, Z., Clapp, J., Xia-Serafino, W., and Cerezo, F.: Sensing heavy precipitation with GNSS polarimetric radio occultations, Geophysical Research Letters, 46, 1024–1031, https://doi.org/10.1029/2018GL080412, 2019.

Cazenave, Q., Ceccaldi, M., Delanoë, J., Pelon, J., Groß, S., and Heymsfield, A. J.: Evolution of DARDAR-CLOUD ice cloud retrievals: New parameters and impacts on the retrieved microphysical properties, Atmospheric Measurement Techniques, 12, 2819–2835, https://doi.org/10.5194/amt-12-2819-2019, 2019.

Davis, C. P., Wu, D. L., Emde, C., Jiang, J. H., Cofield, R. E., and Harwood, R. S.: Cirrus induced polarization in 122 GHz aura Microwave Limb Sounder radiances, Geophysical Research Letters, 32, 1–4, https://doi.org/10.1029/2005GL022681, 2005.

Defer, E., Galligani, V. S., Prigent, C., and Jimenez, C.: First observations of polarized scattering over ice clouds at close-to-millimeter wavelengths (157 GHz) with MADRAS on board the Megha-Tropiques mission, Journal of Geophysical Research: Atmospheres, 119, 12,301–12,316, https://doi.org/10.1002/2014JD022353, 2014.

Delanoë, J. and Hogan, R. J.: A variational scheme for retrieving ice cloud properties from combined radar, lidar, and infrared radiometer, Journal of Geophysical Research Atmospheres, 113, 1–21, https://doi.org/10.1029/2007JD009000, 2008.

Delanoë, J. and Hogan, R. J.: Combined CloudSat-CALIPSO-MODIS retrievals of the properties of ice clouds, Journal of Geophysical Research, 115, D00H29, https://doi.org/10.1029/2009JD012346, 2010.

Draine, B. T. and Flatau, P. J.: Discrete-dipole approximation for scattering calculations, Journal of the Optical Society of America A, 11, 1491, https://doi.org/10.1364/JOSAA.11.001491, 1994.

Gong, J. and Wu, D. L.: Microphysical properties of frozen particles inferred from Global Precipitation Measurement (GPM) Microwave Imager (GMI) polarimetric measurements, Atmospheric Chemistry and Physics, 17, 2741–2757, https://doi.org/10.5194/acp-17-2741-2017, 2017.

Gong, J., Zeng, X., Wu, D. L., Munchak, S. J., Li, X., Kneifel, S., Liao, L., and Barahona, D.: Linkage among Ice Crystal Microphysics, Mesoscale Dynamics and Cloud and Precipitation Structures Revealed by Collocated Microwave Radiometer and Multi-frequency Radar Observations, Atmospheric Chemistry and Physics, 20, 12 633–12 653, https://doi.org/10.5194/acp-20-12633-2020, 2020.

Hajj, G. A., Kursinski, E. R., Romans, L. J., Bertiger, W. I., and Leroy, S. S.: A Technical Description of Atmospheric Sounding By Gps occultation, Journal of Atmospheric and solar-terrestrial physics, 64, 451–469, https://doi.org/10.1016/S1364-6826(01)00114-6, 2002.

Jameson, A. R.: Microphysical Interpretation of Multiparameter Radar Measurements in Rain. Part III: Interpretation and Measurement of Propagation Differential Phase Shift between Orthogonal Linear Polarizations, Journal of the Atmospheric Sciences, 42, 607–614, https://doi.org/10.1175/1520-0469(1985)042<0607:MIOMRM>2.0.CO;2, 1985.

Kaur, I., Eriksson, P., Barlakas, V., Pfreundschuh, S., and Fox, S.: Fast Radiative Transfer Approximating Ice Hydrometeor Orientation and Its Implication on IWP Retrievals, Remote Sensing, 14, 1–33, https://doi.org/10.3390/rs14071594, 2022.

Kursinski, E. R., Hajj, G. A., Schofield, J. T., Linfield, R. P., and Hardy, K. R.: Observing Earth's atmosphere with radio occultation measurements using the Global Positioning System, Journal of Geophysical Research, 102, 23 429–23 465, https://doi.org/10.1029/97JD01569, 1997.

Leinonen, J. and Moisseev, D.: What do triple-frequency radar signatures reveal about aggregate snowflakes ?, Journal of Geophysical Research: Atmospheres, 120, 229–239, https://doi.org/10.1002/2014JD022072, 2015.

Liu, C. and Zipser, E. J.: The global distribution of largest, deepest, and most intense precipitation systems, Geophysical Research Letters, 42, 3591–3595, https://doi.org/10.1002/2015GL063776, 2015.

Liu, G.: A Database of Microwave Single-Scattering Properties for Nonspherical Ice Particles, Bulletin of the American Meteorological Society, 89, 1563–1570, https://doi.org/10.1175/2008BAMS2486.1, 2008.

Mace, G. G., Protat, A., and Benson, S.: Mixed-Phase Clouds Over the Southern Ocean as Observed From Satellite and Surface Based Lidar and Radar, Journal of Geophysical Research: Atmospheres, 126, e2021JD034 569., https://doi.org/10.1029/2021JD034569, 2021.

Marchand, R., Mace, G. G., Ackerman, T., and Stephens, G. L.: Hydrometeor detection using Cloudsat - An earth-orbiting 94-GHz cloud radar, Journal of Atmospheric and Oceanic Technology, 25, 519–533, https://doi.org/10.1175/2007JTECHA1006.1, 2008.

Marshall, J., Donohoe, A., Ferreira, D., and McGee, D.: The ocean's role in setting the mean position of the Inter-Tropical Convergence Zone, Climate Dynamics, 42, 1967–1979, https://doi.org/10.1007/s00382-013-1767-z, 2014.

Maxwell Garnett, J. C.: Colours in Metal Glasses and in Metallic Films, Philosophical transactions of the Royal Society of London, 203, 385–420, https://doi.org/10.1098/rsta.1904.0024, 1904.

Nguyen, C. M., Wolde, M., and Korolev, A. V.: Determination of Ice Water Content (IWC) in tropical convective clouds from X-band dual-polarization airborne radar, Atmospheric Measurement Techniques, 12, 5897–5911, https://doi.org/10.5194/amt-12-5897-2019, 2019.

Oguchi, T.: Electromagnetic wave propagation and scattering in rain and other hydrometeors, Proceedings of the IEEE, 71, 1029–1078, https://doi.org/10.1109/PROC.1983.12724, 1983.

Padullés, R., Ao, C. O., Turk, F. J., de la Torre-Juárez, M., Iijima, B. A., Wang, K. N., and Cardellach, E.: Calibration and Validation of the Polarimetric Radio Occultation and Heavy Precipitation experiment Aboard the PAZ Satellite, Atmospheric Measurement Techniques, 13, 1299–1313, https://doi.org/10.5194/amt-13-1299-2020, 2020.

Padullés, R., Cardellach, E., Turk, F. J., Ao, C. O., de la Torre-Juárez, M., Gong, J., and Wu, D. L.: Sensing Horizontally Oriented Frozen Particles With Polarimetric Radio Occultations Aboard PAZ: Validation Using GMI Coincident Observations and Cloudsat aPriori Information, IEEE Transactions on Geoscience and Remote Sensing, 60, 1–13, https://doi.org/10.1109/TGRS.2021.3065119, 2022.

Ryzhkov, A. V., Zrnić, D. S., and Gordon, B. A.: Polarimetric method for ice water content determination, Journal of Applied meteorology, 37, 125–134, https://doi.org/10.1175/1520-0450(1998)037<0125:PMFIWC>2.0.CO;2, 1998.

Ryzhkov, A. V., Pinsky, M., Pokrovsky, A., and Khain, A. P.: Polarimetric radar observation operator for a cloud model with spectral microphysics, Journal of Applied Meteorology and Climatology, 50, 873–894, https://doi.org/10.1175/2010JAMC2363.1, 2011.

Schneider, T. L., Bischoff, T., and Haug, G. H.: Migrations and dynamics of the intertropical convergence zone., Nature, 513, 45–53, https://doi.org/10.1038/nature13636, 2014.

Stephens, G. L., Vane, D. G., Tanelli, S., Im, E., Durden, S. L., Rokey, M., Reinke, D., Partain, P., Mace, G. G., Austin, R. T., L'Ecuyer, T., Haynes, J., Lebsock, M., Suzuki, K., Waliser, D. E., Wu, D. L., Kay, J., Gettelman, A., Wang, Z., and Marchand, R.: CloudSat mission: Performance and early science after the first year of operation, Journal of Geophysical Research Atmospheres, 113, 1–18, https://doi.org/10.1029/2008JD009982, 2008.

Turk, F. J., Padullés, R., Cardellach, E., Ao, C. O., Wang, K.-N., Morabito, D. D., de la Torre-Juárez, M., Oyola, M., Hristova-Veleva, S. M., and Neelin, J. D.: Interpretation of the Precipitation Structure Contained in Polarimetric Radio Occultation Profiles Using Passive Microwave Satellite Observations, Journal of Atmospheric and Oceanic Technology, 38, 1727–1745, https://doi.org/10.1175/jtech-d-21-0044.1, 2021.

Vivekanandan, J., Bringi, V. N., Hagen, M., and Meischner, P.: Polarimetric radar studies of atmospheric ice particles, IEEE Transactions on Geoscience and Remote Sensing, 32, 1–10, https://doi.org/10.1109/36.285183, 1994.

Wu, D. L., Austin, R. T., Deng, M., Durden, S. L., Heymsfield, A. J., Jiang, J. H., Lambert, A., Li, J. L., Livesey, N. J., McFarquhar, G. M., Pittman, J. V., Stephens, G. L., Tanelli, S., Vane, D. G., and Waliser, D. E.: Comparisons of global cloud ice from MLS, CloudSat, and correlative data sets, Journal of Geophysical Research: Atmospheres, 114, 1–20, https://doi.org/10.1029/2008JD009946, 2009.

Zeng, X., Skofronick-Jackson, G., Tian, L., Emory, A. E., Olson, W. S., and Kroodsma, R. A.: Analysis of the global microwave polarization data of clouds, Journal of Climate, 32, 3–13, https://doi.org/10.1175/JCLI-D-18-0293.1, 2019.